INORGANIC CHEMISTRY

FRONTIERS

Accepted Manuscript

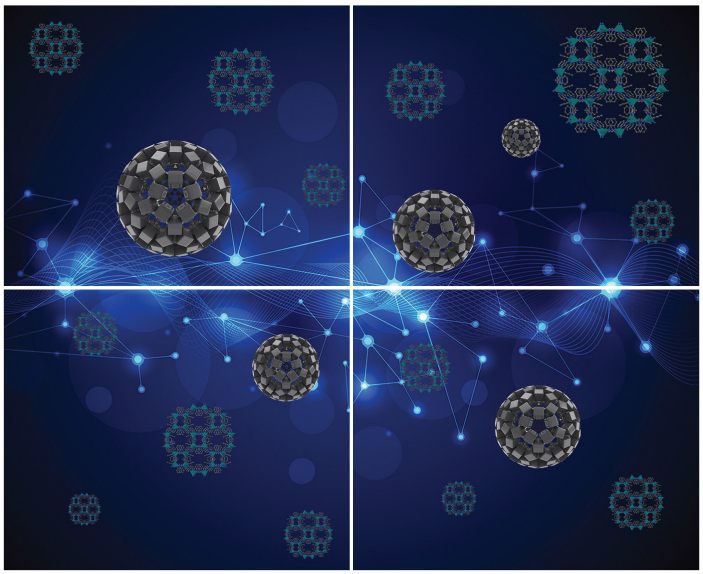

This article can be cited before page numbers have been issued, to do this please use: C. Wei, Y. Liu, X. Li, H. Liu, H. Li, H. Liu and H. Tian, *Inorg. Chem. Front.*, 2025, DOI: 10.1039/D5QI01403D.

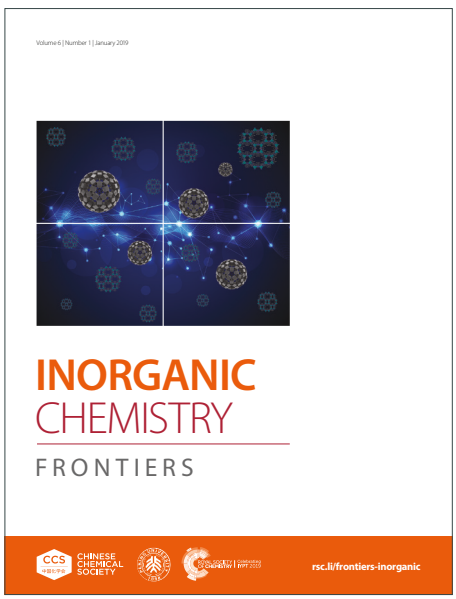

ROYAL SOCIETY OF CHEMISTRY View Article Online
DOI: 10.1039/D5QI01403D

Journal Name

ARTICLE

Pentacosaple-CO_3^{2-} bridged hexacontaoctanuclear lanthanide-alkali barrels derived from octacosanuclear discs†

Received 00th January 20xx,
Accepted 00th January 20xx

DOI: 10.1039/x0xx00000x

www.rsc.org/

Chaolun Wei,[a] Yi Liu,[a] Xiaojuan Li,[a] Haoyu Liu,[a] Hai-Ye Li,*[c] Hou-Ting Liu*[b] and Haiquan Tian*[a]

Phosphonate lanthanide carbonate cages are highly sought after in the development of multifunctional molecular-based materials due to their rigid framework and the inherited properties of metal ions. However, the synergistic coordination of phosphonates and carbonates with lanthanide ions limits their systematic exploration. Here, we developed an efficient method to synthesize the necessary phosphonate lanthanide carbonate compound with a three-shell topology through a stepwise procedure that employs a strategy involving the assembly of several multicomponent systems, aimed at the distinctive C_2-symmetric double hydrazone-based co-ligands. The resulting an octacosanuclear disc $[Dy_{16}K_{12}(\mu_4\text{-}O_3PC_{10}H_7)_2(\mu_5\text{-}O_3PC_{10}H_7)_{12}(\mu_6\text{-}O_3PC_{10}H_7)_2(L^1)_4(\mu_4\text{-}COO)_4(\mu_2\text{-}COO)_2(\mu_3\text{-}O)_4(DMF)_6(MeOH)_2(H_2O)_4]\cdot 8DMF\cdot 4MeCN\cdot 8H_2O$ (**$Dy_{16}K_{12}$**), and an hexacontaoctanuclear barrel $[Dy_{24}Na_{44}(\mu_4\text{-}O_3PC_{11}H_9)_8(\mu_7\text{-}O_3PC_{11}H_9)_8(\mu_7\text{-}CO_3)_{12}(\mu_8\text{-}CO_3)_{13}(L^2)_8(\mu_6\text{-}Cl)_2(\mu_2\text{-}OH)_8(DMF)_8(H_2O)_8]\cdot 2DMF\cdot 6MeOH\cdot 9H_2O$ (**$Dy_{24}Na_{44}$**), were achieved by leveraging the benefits of incorporating mixed chloride and carbonate templating anions along with the replacement of alkali metal ions. In the molecular structure of compound **$Dy_{24}Na_{44}$**, twenty-five carbonate and two chloride anions not only occupy the central cavity of the barrel-shaped framework but also act as crucial bridging units in assembling the molecular topology. Furthermore, the drastic changes in supramolecular structures directly affect magnetic dynamics phenomena, from field-induced complex relaxation phenomenon to zero-field single relaxation phenomenon. This work represents an efficient approach for synthesizing phosphonate lanthanide carbonate cages, thereby broadening the pathway for the ultimate customization of functions.

Introduction

Encouraged by the enzyme binding pockets formed by amino acid residues in biological processes for selective catalysis, the chemical synthesis of high-nuclearity metal compounds with polyhedral cage-like patterns has gained increasing attention in recent years.[1-9] Among these, high-nuclearity lanthanide supramolecules have made significant progress in areas such as chiral induction, catalysis, and magnetic materials.[10-16] Despite these encouraging advancements, there remain numerous synthesis-related challenges that urgently need to be tackled, with the controllable synthesis of coordinating components being a major challenge.

Through a review and analysis of scientific papers published over the past two decades on metal phosphonates and metal carbonates, two key findings emerge: the vast majority of metal phosphonates exhibit extended structures, while the number of molecular cages is relatively small.[17-22] This is primarily due to the multifunctional coordination behavior of phosphonates and their capacity to bond with multiple metal ions, resulting in the formation of metal phosphonates with

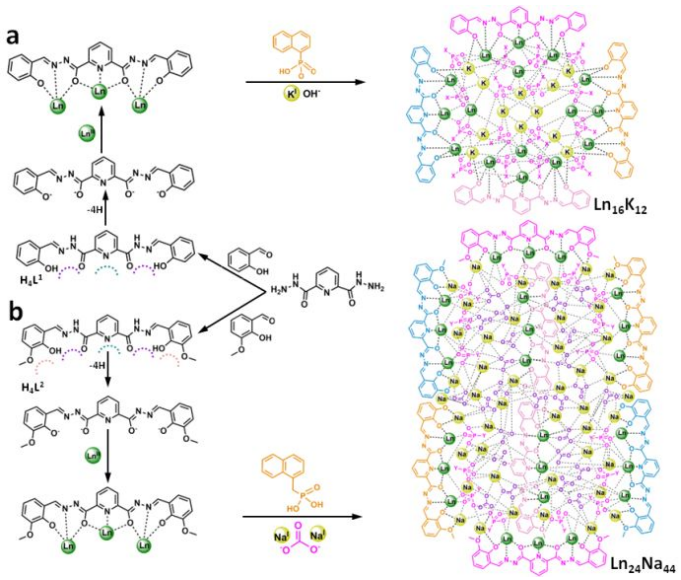

Scheme 1 Graphical representation of **$Dy_{16}K_{12}$** and **$Dy_{24}Na_{44}$**.

carbonate cages, most are formed by the serendipitous fixation of atmospheric CO_2.[23-39] In contrast, instances of one-dimensional, two-dimensional, or three-dimensional

[a] Shandong Provincial Key Laboratory of Chemical Energy Storage and Novel Cell Technology, School of Chemistry and Chemical Engineering, Liaocheng University, Liaocheng 252059, P. R. China. E-mail: tianhaiquan2019@163.com
[b] Food and Biochemistry Engineering Department, Yantai Vocational College, Yantai 264006, P. R. China. E-mail: liuhouting@163.com
[c] Key Laboratory for the Chemistry and Molecular Engineering of Medicinal Resources (Ministry of Education of China), School of Chemistry and Pharmacy, Guangxi Normal University, Guilin, 541004, P. R. China. E-mail: lihaiye2010@163.com
†Electronic Supplementary Information (ESI) available. See DOI: 10.1039/x0xx00000x

DOI: 10.1039/D5QI01482D

structures.[23-28] Among the approximately 130 reported metal synthesizing target compounds by intentionally adding $NaHCO_3$, Na_2CO_3, or other simple carbonates as carbonate bridges are quite rare.[40,41] This rarity is mainly attributed to the rigid structure, specific geometry, and reactivity of carbonate ions in aqueous environments, which often leads to the formation of insoluble and amorphous compounds as the most common reaction pathway.

Due to the coordination tendency of phosphonate and carbonate ligands being difficult to curtail, the development of metal phosphonate/carbonate cages has lagged far behind their extended structures. Chemists are committed to achieving this goal through three synthetic strategies. The first strategy involves designing and synthesizing phosphonate ligands with larger steric hindrance to limit the nuclearity, thereby assembling metal phosphonate cages. The second strategy is to utilize ancillary ligands to block coordination sites on metal ions, thus reducing the likelihood of phosphonate ligands participating in metal assembly. The third strategy is to use metal compounds formed with specific labile ligands as precursors, which, with the assistance of phosphonate ligands, increases the nuclearity.[20,22,25] Strategies 2 and 3 are also applicable to the synthesis of metal carbonate cages.

Our strategy for synthesizing phosphonate lanthanide carbonate cages involves designing bulky 1-naphthylphosphonate and 1-naphthylmethylphosphonate ligands to assist in expanding the simple precursor with C_2-symmetric double hydrazone-based co-ligand pre-assembly. In this process, Na_2CO_3 is intentionally added to provide carbonate anions (Scheme 1), facilitating the encapsulation and synthesis of the target compound. Herein we have succeeded in assembling an octacosanuclear disc $[Dy_{16}K_{12}(\mu_4\text{-}O_3PC_{10}H_7)_2(\mu_5\text{-}O_3PC_{10}H_7)_{12}(\mu_6\text{-}O_3PC_{10}H_7)_2(L^1)_4(\mu_4\text{-}COO)_4(\mu_2\text{-}COO)_2(\mu_3\text{-}O)_4(DMF)_6(MeOH)_2(H_2O)_4]\cdot 8DMF\cdot 4MeCN\cdot 8H_2O$ (**$Dy_{16}K_{12}$**), and a hexacontaoctanuclear barrel $[Dy_{24}Na_{44}(\mu_4\text{-}O_3PC_{11}H_9)_8(\mu_7\text{-}O_3PC_{11}H_9)_8(\mu_7\text{-}CO_3)_{12}(\mu_8\text{-}CO_3)_{13}(L^2)_8(\mu_6\text{-}Cl)_2(\mu_2\text{-}OH)_8(DMF)_8(H_2O)_8]\cdot 2DMF\cdot 6MeOH\cdot 9H_2O$ (**$Dy_{24}Na_{44}$**), where H_4L^1, H_4L^2, $C_{10}H_7PO_3H_2$ and $C_{11}H_9PO_3H_2$ are *N*'^{2},*N*'^{6}-bis((*E*)-2-hydroxybenzylidene)pyridine-2,6-dicarbohydrazide, *N*'^{2},*N*'^{6}-bis((*E*)-2-hydroxy-3-methoxybenzylidene)pyridine-2,6-dicarbohydrazide, 1-naphthylphosphonic acid and 1-naphthylmethylphosphonic acid, respectively. In compound **$Dy_{16}K_{12}$**, sixteen Dy atoms and sixteen phosphonate ligands are separated by twelve potassium atoms in a cross-linked manner, while in compound **$Dy_{24}Na_{44}$**, twenty-four Dy atoms and sixteen phosphonate ligands are separated by forty-four sodium atoms in an outer embedded arrangement. The C_2-symmetric double hydrazones play a role in truncating the co-ligands during the assembly process by introducing different substituents. Compound **$Dy_{24}Na_{44}$** encapsulates twenty-five carbonate anions and two chloride ions, with the proportion of carbonate being the highest reported in cluster compounds to date. The changes in the cage-shaped cores based on the phosphonate lanthanide carbonate units directly lead to complex slow relaxation phenomena and significantly expand the structural diversity of the three-shell coordination clusters.

Table 1. Summary of crystallographic and refinement data for **$Dy_{16}K_{12}$** and **$Dy_{24}Na_{44}$**.

Compound	$Dy_{16}K_{12}$	$Dy_{24}Na_{44}$	Compound	$Dy_{16}K_{12}$	$Dy_{24}Na_{44}$
formula	$C_{302}H_{304}Dy_{16}K_{12}N_{38}O_{108}P_{16}$	$C_{421}H_{410}Cl_2Dy_{24}Na_{44}N_{50}O_{212}P_{16}$	Z	18	2
M_r	9758.59	15040.01	ρ[g cm^{-3}]	1.289	1.546
cryst size [mm^3]	0.15 × 0.14 × 0.14	0.13 × 0.12 × 0.12	2ϑ[deg]	3.5 – 66.6	1.6 –66.6
T [K]	100.00(12)	100.00(10)	F(000)	77076	14112
crystal system	Trigonal	Tetragonal	reflns collected	860476	162226
space group	*R*-3*c* #167	*P*4/*n* #85	unique reflns	40336	27537
a [Å]	48.8720(1)	34.0254(1)	R_{int}	0.132	0.099
b [Å]	48.8720(1)	34.0254(1)	GOF	1.01	1.06
c [Å]	99.4107(3)	26.9880(2)	$R1$ [I> 2σ(I)][a]	0.0507	0.0696
α [°]	90	90	w$R2$ (all data)[b]	0.1513	0.1937
β[°]	90	90	$(\Delta\rho)_{max}$, $(\Delta\rho)_{min}$/[e Å^{-3}]	2.41, -0.89	2.65, -1.73
γ [°]	120	90	CCDC number	2456379	2456380
V [Å^3]	205628.7(10)	31244.8(3)			

Experimental section

Syntheses of the phosphonate ligands: 1-naphthylphosphonic acid ($C_{10}H_7PO_3H_2$) and 1-naphthylmethylphosphonic acid ($C_{11}H_9PO_3H_2$) were synthesized as the literature method.[42,43]

Synthesis of *N*'^{2},*N*'^{6}-bis((*E*)-2-hydroxybenzylidene)pyridine-2,6-dicarbohydrazide (H_4L^1). Pyridine-2,6-dicarbohydrazide (3.9036 g, 20 mmol) was suspended with 2-hydroxybenzaldehyde (4.8848 g, 40 mmol) in MeOH (50 mL), and then the mixed solution was stirred for 24 h at ambient temperature. Pale yellow solid was obtained through filtration, yielding 76%. Elemental analysis (%) calcd for $C_{21}H_{17}N_5O_4$: C, 62.53, H, 4.25, N, 17.36: found C, 61.72, H, 4.10, N, 16.94. IR (KBr, cm^{-1}): 3302(m), 3274(w), 1697(vs), 1682(vs), 1611(w), 1593(m), 1571(m), 1529(s), 1489(w), 1446(m), 1364(w),

1297(m), 1271(s), 1256(w), 1206(m), 1158(w), 1120(m), 1088(m), 1032(m), 1001(w), 955(w), 919(m), 870(s), 844(m), 776(w), 752(s), 647(m), 567(m), 481(m), 426(m).

Synthesis of *N*'^{2},*N*'^{6}-bis((*E*)-2-hydroxy-3-methoxybenzylidene) pyridine-2,6-dicarbohydrazide (H_4L^2). Pyridine-2,6-dicarbohydrazide (3.9036 g, 20 mmol) was suspended with 2-hydroxy-3-methoxybenzaldehyde (6.0861 g, 40 mmol) in MeOH (50 mL), and then the mixed solution was stirred for 24 h at ambient temperature. Pale yellow solid was obtained through filtration, yielding 91%. Elemental analysis (%) calcd for $C_{23}H_{21}N_5O_6$: C, 59.61, H, 4.57, N, 15.11: found C, 57.98, H, 4.51, N, 14.86. IR (KBr, cm^{-1}): 3457(w), 3242(w), 1673(vs), 1654(s), 1608(w), 1590(w), 1577(w), 1541(vs), 1460(s), 1446(w), 1367(w), 1302(w), 1251(vs), 1235(m), 1168(w), 1080(s), 999(m), 988(m), 944(m), 886(w), 836(w), 775(w), 732(s), 653(w), 524(m).

Synthesis of $[Dy_{16}K_{12}(\mu_4\text{-}O_3PC_{10}H_7)_2(\mu_5\text{-}O_3PC_{10}H_7)_{12}(\mu_6\text{-}O_3PC_{10}H_7)_2(L^1)_4(\mu_4\text{-}COO)_4(\mu_2\text{-}COO)_2(\mu_3\text{-}O)_4(DMF)_6(MeOH)_2(H_2O)_4]\cdot 8DMF\cdot 4MeCN\cdot 8H2O$ ($Dy_{16}K_{12}$). A mixture of $C_{10}H_7PO_3H_2$ (0.0375 g, 0.18 mmol) and dysprosium perchlorate hexahydrate (0.1422 g, 0.25 mmol) in 30 mL of a 2:2:1 DMF/MeOH/MeCN mixture was heated with potassium hydroxide (0.0101 g, 0.18 mmol) at 100 °C. After 5 h, H_4L^1 (0.0605 g, 0.15 mmol) was gradually added to the resulting pale-yellow solution to generate a yellow solution. The solution is transferred to a Teflon-lined autoclave and placed in a drying oven to crystallize at 100 °C. Pale-yellow plates were isolated in 41% yield after 15 days. Elemental analysis (%) calcd for $C_{302}H_{304}Dy_{16}K_{12}N_{38}O_{108}P_{16}$: C, 37.17, H, 3.14, N, 5.46: found C, 36.52, H, 3.06, N, 5.39. IR (KBr, cm^{-1}): 3415(w), 3052(m), 2929(m), 1658(vs), 1614(w), 1566(w), 1539(w), 1505(m), 1472(s), 1447(w), 1384(m), 1344(m), 1252(m), 1200(m), 1180(m), 1149(s), 1097(vs), 1068(vs), 1013(s), 968(w), 902(w), 828(m), 801(w), 776(w), 758(w), 676(w), 626(m), 601(m), 584(s), 573(w), 551(m), 518(w), 490(w), 465(m), 459(m), 441(m).

Synthesis of $[Dy_{24}Na_{44}(\mu_4\text{-}O_3PC_{11}H_9)_8(\mu_7\text{-}O_3PC_{11}H_9)_8(\mu_6\text{-}CO_3)_8(\mu_7\text{-}CO_3)_{12}(\mu_8\text{-}CO_3)_{13}(L^2)_8(\mu_6\text{-}Cl)_2(\mu_2\text{-}OH)_8(DMF)_8(H_2O)_8]\cdot 2DMF\cdot 6MeOH\cdot 9H_2O$ ($Dy_{24}Na_{44}$). A mixture of $C_{11}H_9PO_3H_2$ (0.0399 g, 0.18 mmol) and dysprosium perchlorate hexahydrate (0.1422 g, 0.25 mmol) in 30 mL of a 2:2:1 DMF/MeOH/MeCN mixture was heated with sodium hydroxide (0.0072 g, 0.18 mmol) at 100 °C. After 5 h, H_4L^2 (0.0695 g, 0.15 mmol), sodium chloride (0.0058 g, 0.10 mmol) and sodium carbonate (0.0105 g, 0.10 mmol) was gradually added to the resulting yellow solution to generate a yellow-orange solution. The solution is transferred to a Teflon-lined autoclave and placed in a drying oven to crystallize at 100 °C. Yellow pillars were isolated in 24% yield after 10 days. Elemental analysis (%) calcd for $C_{421}H_{410}Cl_2Dy_{24}Na_{44}N_{50}O_{212}P_{16}$: C, 33.62, H, 2.75, N, 4.66: found C, 32.59, H, 2.61, N, 4.45. IR (KBr, cm^{-1}): 3416(w), 3049(m), 2927(m), 1612(vs), 1566(s), 1468(s), 1396(m), 1357(w), 1338(m), 1271(m), 1236(w), 1218(vs), 1168(m), 1104(vs), 1069(vs), 1018(w), 984(s), 948(w), 860(w), 831(m), 801(m), 779(w), 738(w), 689(m), 670(m), 644(m), 560(m), 504(m).

Results and discussion

Structure information. Dysprosium perchlorate was dissolved in a 2:2:1 mixture of DMF, MeOH, and MeCN. The assembly process from the disc-shaped octacosanuclear **$Dy_{16}K_{12}$** to the barrel-shaped hexacontaoctanuclear **$Dy_{24}Na_{44}$** involves four key changes: First, $C_{11}H_9PO_3H_2$ was used to replace $C_{10}H_7PO_3H_2$, introducing the rotatability of the P-C bond, which makes the phosphonate ligand easier to adjust its coordination position around the lanthanide cage; second, H_4L^2 replaced H_4L^1, and the introduction of dimethoxy groups further extended the C_2-symmetric double hydrazone coordination sites, thereby expanding the structure of the lanthanide cage; third, sodium hydroxide was used instead of potassium hydroxide, and the reduction in alkalinity slowed the deprotonation rate of the phosphonate and the hydrazone ligands, facilitating the formation of the high-nuclearity lanthanide cage; finally, additional sodium carbonate and sodium chloride were added, and the introduction of the mixed templating anions not only participated in the construction of the lanthanide cage but also embedded into the central cavity of the cage based on a certain directive function during the synthesis process.

The octacosanuclear disc **$Dy_{16}K_{12}$** crystallizes in the trigonal $R\bar{3}c$ space group (number 167), with unit cell volume of 2.06 × 10^5 Å^3 (Table 1). As shown in Figure 1 and S6, despite the very large unit cell volume, the corresponding asymmetric unit is relatively small. Compound **$Dy_{16}K_{12}$** is as large as 25.19 × 25.19 Å^2 with height of 19.12 Å, featuring novel three-shell cyclic core structure and possessing a threefold axis of symmetry (Figure 1a and S6a). The complete molecule consists of the disc-shaped cationic core $[Dy_{16}K_{12}(\mu_4\text{-}COO)_4(\mu_2\text{-}COO)_2(\mu_3\text{-}O)_4]^{40+}$, $16C_{10}H_7PO_3H_2$ ligands, $4H_4L^1$ co-ligands, 6DMF molecules, together with 2 molecules of MeOH and 4 water molecules. A further detailed analysis of this structure reveals a sequence of layers arranged from the inside out: the innermost layer is a cubane-shaped K_4O_4 unit formed by two K1 and two K2 atoms connected by four formate groups and eight phosphonate oxygen atoms (Figure 1d and S7a). The middle layer is a bowl-shaped Dy_4K_4 unit, constructed from four identical parts connected in a welding manner, with each part containing two Dy atoms (Dy3 and Dy4) and one K3 atom. These Dy and K atoms are interconnected by forty phosphonate oxygen atoms (Figure S7b). The outermost $Dy_{12}K_4$ unit can be simplified into a ring structure composed of four fan-shaped structures. Each fan-shaped structure is formed by three Dy atoms (Dy5, Dy6, Dy7) and two K atoms (K4, K5) interconnected by thirty phosphonate oxygen atoms (Figure 1d).

The four outermost C_2-symmetric double hydrazones chelate three Dy atoms through their tetradeprotonated forms *via* three larger internal coordination pockets, while bridging two K atoms using the smaller coordination pockets at both ends,

a b c

View Article Online
DOI: 10.1039/D5QI01403D

Journal Name

ARTICLE

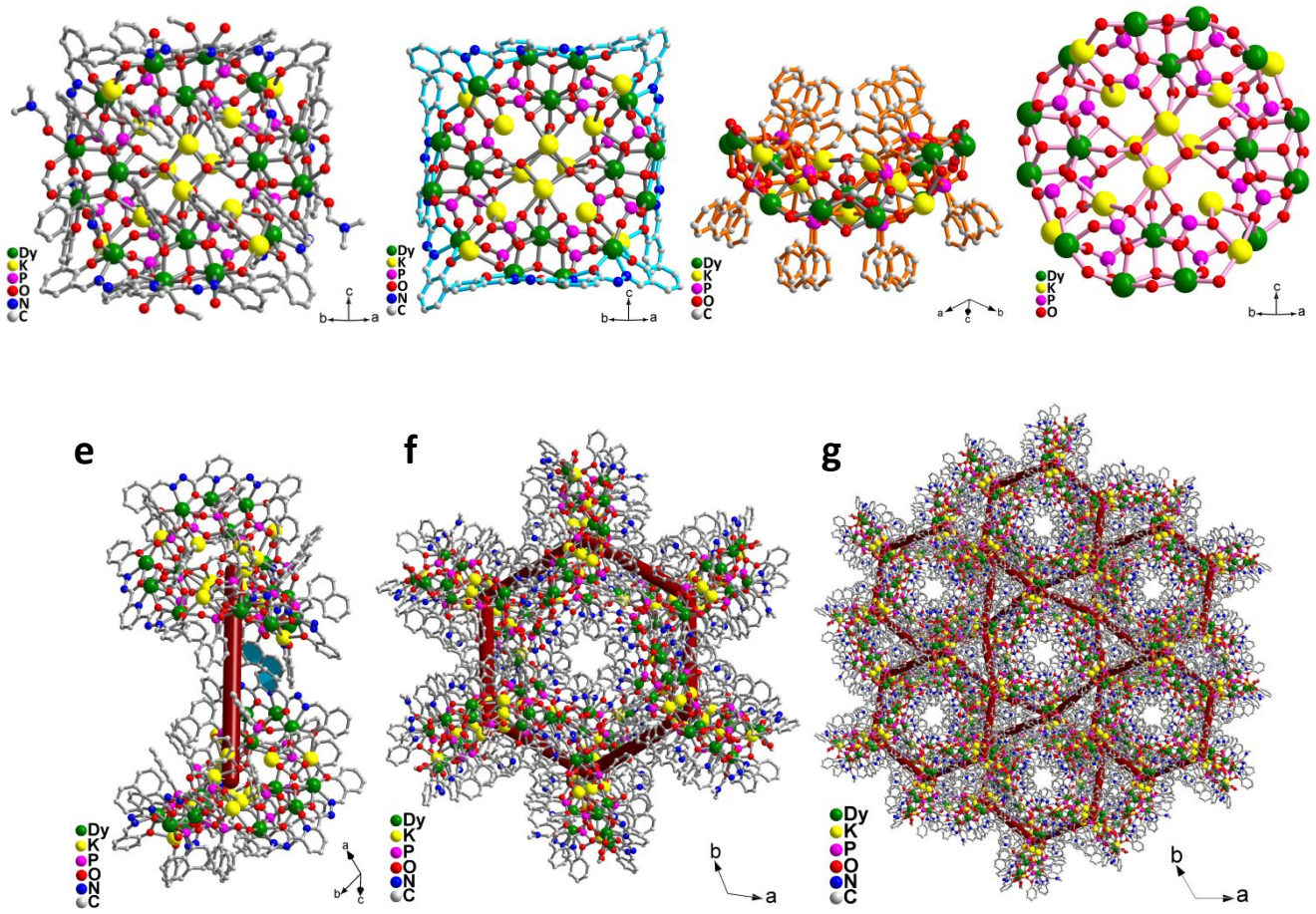

Figure 1. Ball and stick view of **$Dy_{16}K_{12}$** (a).Highlighting four L^1 ligands (b) and sixteen $C_{10}H_7PO_3^{2-}$ ligands (c). The $[Dy_{16}K_{12}(O_3P)_{16}(\mu_4\text{-}COO)_4(\mu_3\text{-}O)_4(\mu_2\text{-}O)_{12}]^{28+}$ core (d). The coordinating water, methanol and DMF molecules are omitted. The rod-shaped linker mode connects the nearest two molecules through π-π interactions (e). Three-shell cyclic clusters assembled into a six-membered ring (f). The ultimate two-dimensional Kagomé topology (g).

adopting the same μ_5-η^2:η^1:η^2:η^1:η^2:η^1:η^2 coordination modes (Figure 1b and S8a). This essentially acts as an inhibiting co-ligand, effectively preventing the formation of dysprosium phosphonate coordination polymers. Simultaneously, this suggests that if such hydrazones can be rationally designed, it may be possible to control the aggregation and growth of disc-shaped compounds.

Hexadecaple phosphonate ligands are alternately arranged in a plane between the outer layer and the middle layer, exhibiting three distinct coordination modes (Figure 1c and S8b): The first is μ_4-$C_{10}H_7PO_3^{2-}$, which coordinates with three Dy atoms and one K atom, presenting a μ_4-η^1:η^1:η^2 coordination mode, involving 2 phosphonate ligands; the second is μ_5-$C_{10}H_7PO_3^{2-}$, which coordinates with three Dy atoms and two K atoms, displaying a μ_5-η^1:η^2:η^2 coordination mode, involving 12 phosphonate ligands; the third is μ_6-$C_{10}H_7PO_3^{2-}$, which coordinates with four Dy atoms and two K atoms, demonstrating a μ_6-η^1:η^2:η^3 coordination mode, involving 2 phosphonate ligands.

Despite the presence of up to eight crystallographically independent Dy atoms in the asymmetric unit, the coordination numbers of these Dy atoms are only eight and nine. Analysis using CShM software[44,45] revealed three types of coordination geometries. Specifically, the four Dy atoms in the middle layer exhibit a triangular dodecahedron (D_{2d}) with an O_7 environment, the eight Dy atoms at the outer layer connection points display a pentagonal bipyramid (D_{5h}) with an O_8 environment, while the four Dy atoms at the outer layer vertices

present a biaugmented trigonal prism (C_{2v}) with an NO_7 environment (Figure S7b and Table 2 and S5).

Further analysis of the crystal packing structure reveals that two adjacent molecules are positioned face-to-face, with the naphthyl groups of the phosphonate ligands aligned parallel to the pyridinyl groups of the H_4L^1 ligands, exhibiting an average centroid-to-centroid distance of 3.8767(1) Å and an interplane angle of 7.698°, indicative of π-π stacking interactions. These π-π interactions form rod-shaped linkages (Figure 1e) that assemble into chair six-membered rings (Figure 1f). The chair six-membered rings stack along the crystallographic c-axis, ultimately generating a two-dimensional Kagomé topology (Figure 1g).[46]

The **$Dy_{16}K_{12}$** core exhibits significant differences in local

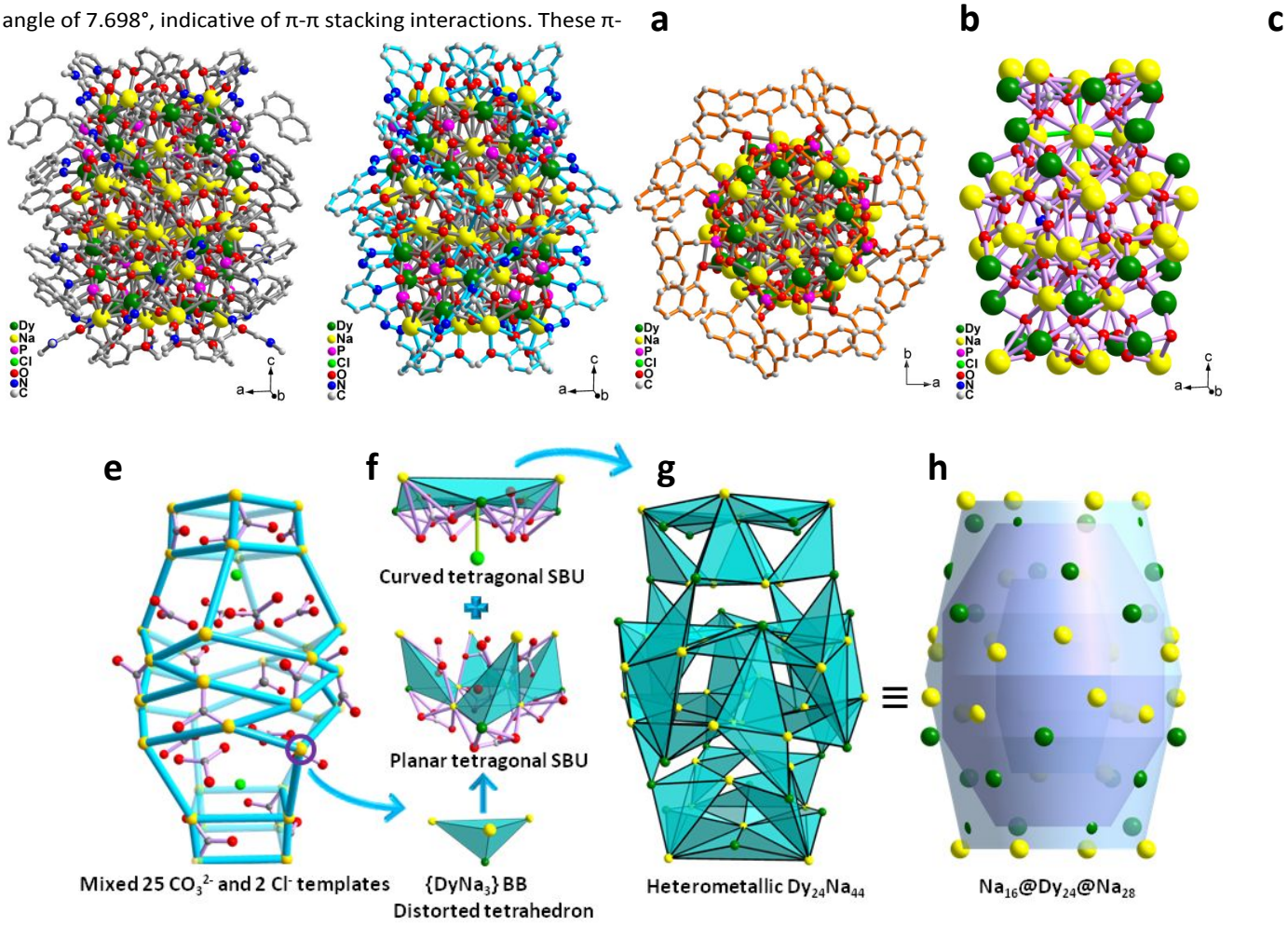

Figure 2. Ball and stick view of **$Dy_{24}Na_{44}$** (a).Highlighting eight L^2 (b) and sixteen $C_{11}H_9PO_3^{2-}$ ligands (c). The $[Dy_{24}Na_{44}(\mu_7\text{-}CO_3)_{12}(\mu_8\text{-}CO_3)_{13}]^{66+}$ core (d). The coordinating water, methanol and DMF molecules are omitted. The barrel-shaped framework of the anion-templated cluster showing the CO_3^{2-} and Cl^- templates (e). The heterometallic planar and curved tetragonal SBUs derived from the [$DyNa_3$] BB (f). The core structure of **$Dy_{24}Na_{44}$** showing its vertex- and edge-sharing tetrahedral BBs (g). The three-shell structure of **$Dy_{24}Na_{44}$** with the showing of its barrel-shaped structural correlation (h).

symmetry between the inner and outer layers: the K_4 in the inner layer and the Dy_4K_4 square wheel in the middle layer display approximately D_{4h} local symmetry, while the outer layer $Dy_{12}K_4$ shows C_{4v} symmetry. This difference suggests that the symmetry breaking may be a crucial factor in inhibiting the further growth of the cyclic coordination clusters.[47] Additionally, the increase in surface tension ultimately suppresses the epitaxial growth of the core. The H_4L^1 co-ligand coordinates with the outer layer of Dy and K atoms around the core in a head-to-tail manner, effectively truncating growth; meanwhile, $C_{10}H_7PO_3H_2$ ligand alternates as a cap between the outer and inner layer's annular region. Since the naphthyl group is directly connected to the P atom of the phosphonate ligand, its flexibility is significantly restricted. Consequently, we modified the ligand structure: incorporating ortho-methoxy substituents on both sides of the H_4L^1 co-ligand, and replacing $C_{10}H_7PO_3H_2$ ligand with $C_{11}H_9PO_3H_2$ ligand; simultaneously, KOH was substituted with Na_2CO_3 to incorporate carbonate anion templates, complemented by a chloride anion template. This ultimately led to the successful isolation of another type of yellow pillar-like crystal, indicating the formation of a new metallosupramolecular aggregate.

The hexacontaoctanuclear barrel **$Dy_{24}Na_{44}$** crystallizes in the tetragonal *P*4/*n* space group (number 85), with unit cell volume

View Article Online
DOI: 10.1039/D5QI01403D

of 3.12×10^4 Å^3 (Table S1). As shown in Figure S14, compound **$Dy_{24}Na_{44}$** is as large as 29.59×29.59 Å^2 with height of 26.44 Å, featuring novel three-shell barrel-shaped core structure and possessing a fourfold axis of symmetry. The complete molecule consists of the barrel-shaped cationic core $[Dy_{24}Na_{44}(\mu_7\text{-}CO_3)_{12}(\mu_8\text{-}CO_3)_{13}(\mu_6\text{-}Cl)_2(\mu_2\text{-}OH)_8]^{56+}$, $16C_{11}H_9PO_3H_2$ ligands, $8H_4L^2$ co-ligands, 8DMF molecules and 8 water molecules (Figure 2a). Compared to the H_4L^1 co-ligand, the H_4L^2 co-ligand incorporates methoxy groups at both sides, which chelate three Dy atoms in the three large coordination pockets in the internal while the two carboxylate oxygen atoms further bridge two Na atoms. The two small coordination pockets formed by the two terminal methoxy and phenolic hydroxyl groups chelate an additional two Na atoms, exhibiting a μ_7-η^1:η^2:η^1:η^3:η^1:η^3:η^1:η^2:η^1 coordination mode (Figure 2b and S11a). This structure can still act as a co-ligand to inhibit the formation of dysprosium phosphonate coordination polymers, but its inhibitory effect is significantly weaker than that of the H_4L^1 co-ligand. Additionally, the H_4L^2 co-ligand plays a role in suppressing the formation of carbonate coordination polymers and/or insoluble compounds, which is also the direct reason for the isolation of the **$Dy_{24}Na_{44}$** compound.

Although compound **$Dy_{24}Na_{44}$** has the same number of hexadecaple phosphonate ligands as compound **$Dy_{16}K_{12}$**, the flexible modification of the naphthyl groups of the the phosphonate ligands results in a $4 \times 4 \times 4 \times 4$ vertical distribution pattern of its $C_{11}H_9PO_3H_2$ ligands (Figure 2c and S11b). These ligands exhibit only two coordination modes: the first involves eight μ_4-$C_{11}H_9PO_3^{2-}$ located at the top and bottom of the barrel-shaped structure, coordinating in a μ_4-η^1:η^2:η^2 fashion (three Dy and one Na atoms); the second involves eight μ_7-$C_{11}H_9PO_3^{2-}$ located in the middle of the barrel-shaped structure, coordinating in a μ_7-η^2:η^3:η^3 fashion (three Dy and four Na atoms).

Table 2. Summary of coordination geometries of the dysprosium atoms and bonding modes of the components in **$Dy_{16}K_{12}$** and **$Dy_{24}Na_{44}$**.

compound	$Dy_{16}K_{12}$	$Dy_{24}Na_{44}$
Formula	$[Dy_{16}K_{12}(\mu_4\text{-}O_3PC_{10}H_7)_2(\mu_5\text{-}O_3PC_{10}H_7)_{12}(\mu_6\text{-}O_3PC_{10}H_7)_2(L^1)_4(\mu_4\text{-}COO)_4(\mu_2\text{-}COO)_2(\mu_3\text{-}O)_4(DMF)_6(MeOH)_2(H_2O)_4]\cdot 8DMF\cdot 4MeCN\cdot 8H_2O$	$[Dy_{24}Na_{44}(\mu_4\text{-}O_3PC_{11}H_9)_8(\mu_7\text{-}O_3PC_{11}H_9)_8(\mu_7\text{-}CO_3)_{12}(\mu_8\text{-}CO_3)_{13}(L^2)_8(\mu_6\text{-}Cl)_2(\mu_2\text{-}OH)_8(DMF)_8(H_2O)_8]\cdot 2DMF\cdot 6MeOH\cdot 9H_2O$
Phosphonate	2 μ_4-η^1:η^1:η^2, 12 μ_5-η^1:η^2:η^2, 2 μ_6-η^1:η^2:η^3	8 μ_4-η^1:η^2:η^2, 8 μ_7-η^2:η^3:η^3
Carbonate	--	12 μ_7-η:$^2\eta$:$^3\eta^3$, 13 μ_8-η:$^3\eta$:$^3\eta^3$
Hydrazone	4 μ_5-η^2:η^1:η^2:η^1:η^2:η^1:η^2	8 μ_7-η^1:η^2:η^1:η^3:η^1:η^3:η^1:η^2:η^1
Coordination Geometries	2 BTPR-8 (C_{2v}), 2 COC-7 (C_{3v}), 2 PBPY-7 (D_{5h}), 2 TDD-8 (D_{2d})	2 BTPR-8 (C_{2v}), 1 CSAPR-9 (C_{4v}), 1 MFF-9 (C_s), 2 TDD-8 (D_{2d}),

More importantly, by proactively adopting Na_2CO_3 as a replacement for KOH, we successfully encapsulated 25 CO_3^{2-} anions within the barrel-shaped structure of compound **$Dy_{24}Na_{44}$** (Figure 2d and S13). Based on the following three pieces of evidence, we identified the coordination modes of these CO_3^{2-} anions: (i) 25 distinct trigonal fragments were clearly observed in the diffraction data; (ii) these sites requires 25 dianions to maintain electrical neutrality; (iii) characteristic infrared stretching bands of coordinated carbonates were detected at 1566 cm^{-1} and 1338 cm^{-1} (Figure S2b).[48] These anions exhibited a vertical gradient distribution of 6 × 13 × 6: the carbonate anion (twelve) located at the top and bottom of the barrel-shaped structure bridges three Dy and four Na atoms using a μ_7-η:$^2\eta$:$^3\eta$:η^3 heptadentate coordination mode. The carbonate anion (thirteen) positioned in the middle of the structure adopt a μ_8-η:$^3\eta$:$^3\eta$:η^3 octadentate coordination mode, connecting one Dy and seven Na atoms. Therefore, the incorporation of twenty-five carbonate anions into the structure effectively guided and accelerated the subsequent aggregation and growth of the cluster.

In-depth analysis of this complex high-nuclear structure requires a systematic deconstruction of the three-layered, barrel-shaped polyhedral core supported by carbonate and chloride (Figure 2e and S15), based on {$DyNa_3$} building blocks (BBs). Each {$DyNa_3$} BB is arranged with vertex-sharing, forming two planar tetragonal heterometallic secondary building units (SBUs) connected by octuple CO_3^{2-} bridges; when arranged with edge-sharing, it results in four curved tetragonal heterometallic SBUs linked by quadruple CO_3^{2-} and single Cl^- bridges (Figure 2f). These two types of SBUs alternate to ultimately form a three-shell barrel-shaped topology (Figure 2g and 2h). The following considerations apply from the inside to the outside: (i) The innermost layer consists of sixteen Na atoms linked by two μ_6-Cl atoms, twelve carbonate oxygen atoms, and eight μ_2-O oxygen atoms, forming a $Na_{16}Cl_2O_{28}$ barrel-shaped core (illustrated in inner turquiose in Figure 2g); (ii) the middle layer is constructed from twenty-four Dy atoms linked by thirty-six carbonate oxygen atoms, thirty-two phosphonate oxygen atoms, and sixteen hydrazone carboxylate oxygen atoms from the H_4L^2 ligands, resulting in a $Dy_{24}O_{84}$ barrel-shaped core (illustrated in middle violet in Figure 2g); (iii) the outer $Na_{28}O_{60}$ barrel core (illustrated in outer turquiose in Figure 2g) is formed through cross-linking of twenty-eight Na atoms with twenty-four carbonate oxygen atoms, sixteen phosphonate oxygen atoms, and sixteen hydrazone phenolato oxygen atoms from the H_4L^2 ligands.

In contrast to Compound **$Dy_{16}K_{12}$**, although the number of central Dy atoms increases from 16 to 24, the number of Dy atoms in the asymmetric unit decreases from 8 to 6. These Dy atoms exhibit only coordination numbers of eight and nine and display three different coordination geometries (Figure S12b): the eight Dy atoms located at the top and bottom of the barrel-shaped structure exhibit a

triangular dodecahedron (D_{2d}) with an NO_7 environment, the eight Dy atoms at the connecting sides exhibit a muffin (C_s) with an NO_8 environment, while the eight Dy atoms in the center exhibit a biaugmented trigonal prism (C_{2v}) with an NO_7 environment. Despite the doubling of the number of hydrazone co-ligands, the deeper analysis of the crystal packing structure did not observe the formation of supramolecular polymers due to the changes in the flexibility of the phosphonate ligands.

The most prominent structural feature of these two giant **$Dy_{16}K_{12}$** and **$Dy_{24}Na_{44}$** cages lies in the key differences among the phosphonate ligands surrounding the structure, the terminal C_2-symmetric double hydrazone-based co-ligands, and the mixed templating anions. This feature indicates that precise control over the size of the cage can be achieved by regulating the relative proportions of the three components. This strategy is a classic method for modifying crystal morphology,[49-51] just as the selective addition of additives to rapidly growing faces of polyhedral crystals can expand the diameter of the cages and increase the ligand content, attempts to isolate larger-sized cages at various ratios have been unsuccessful. It is important to note that the flexibility and steric hindrance of the R groups in the phosphonate ligands and hydrazone co-ligands, along with the selection of mixed templating anions, play a crucial role in the construction of the final structure. Essentially, the electrostatically dominated coordination interactions between the lanthanides and the ligands take precedence, while the π–π interactions between the naphthyl groups of the phosphonate ligands and the pyridyl groups of the hydrazone co-ligands operate in synergy, facilitating the transformation from a three-shell cyclic structure to a three-shell barrel-shaped structure.

***DC* magnetic properties.** After a comprehensive structural elucidation of the rare octacosanuclear and hexacontaoctanuclear metallosupramolecular assemblies, we systematically examined their magnetic properties and assessed their potential as high-nuclearity Ln-SMMs.[21,52-59] The temperature-dependent magnetic susceptibility of **$Dy_{16}K_{12}$** and **$Dy_{24}Na_{44}$** was performed on microcrystalline sample in a 1.0 kOe dc magnetic field (Figure S16). At room temperature, their $\chi_M T$ values were 224.91 (**$Dy_{16}K_{12}$**) and 336.86 (**$Dy_{24}Na_{44}$**) emu·K/mol, respectively, which align with the theoretical expected values for sixteen and twenty-four free Dy(III) ions (S = 5/2, L = 5, $^6H_{15/2}$, C = 14.17 emu·K/mol with g = 4/3). As the temperature was cooled to 56 K, the $\chi_M T$ values gradually decreased to 208.27 (**$Dy_{16}K_{12}$**) and 307.69 (**$Dy_{24}Na_{44}$**) emu·K/mol, and continued to decline rapidly with further cooling, reaching a

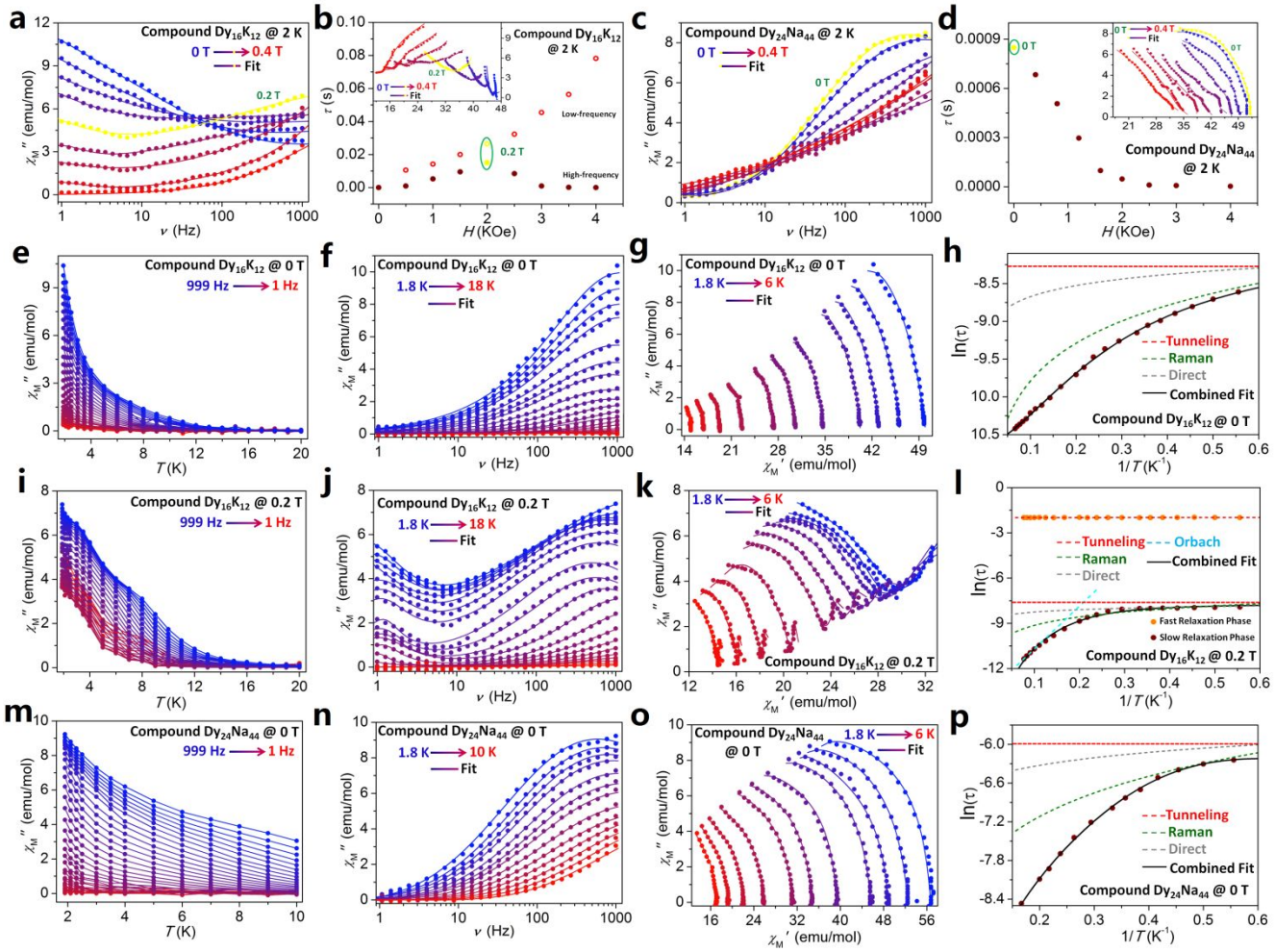

Figure 3. Out-of-phase component of the magnetic susceptibility (χ_M'') for **$Dy_{16}K_{12}$** (a) and **$Dy_{24}Na_{44}$** (c) collected under different external dc field. Plots of

magnetic relaxation time τ versus H for **$Dy_{16}K_{12}$** (b) and **$Dy_{24}Na_{44}$** (d). Cole-Cole plots for **$Dy_{16}K_{12}$** (b, inset) and **$Dy_{24}Na_{44}$** (d, inset). Data were collected at the temperatures of 0 T to 0.4 T. The solid lines represent fits to the data using the generalized Debye model with two-step or one-step relaxation profiles. $\chi_M''(\nu)$ plots for **$Dy_{16}K_{12}$** (e, f, i, j) and **$Dy_{24}Na_{44}$** (m, n) collected under zero and 0.2 T applied dc field. Cole-Cole plots for **$Dy_{16}K_{12}$** (g, k) and **$Dy_{24}Na_{44}$** (o). Data were collected at the temperatures of 1.8 K to 6 K. Plots of magnetic relaxation time ln(τ) versus 1/T for **$Dy_{16}K_{12}$** (h, l) and **$Dy_{24}Na_{44}$** (p). Turquoise, green, gray and red dashed lines represent individual Orbach, Raman, Direct and quantum tunneling fits. Black lines represent the overall fits, as described in the main text.

minimum of 139.09 (**$Dy_{16}K_{12}$**) and 208.96 (**$Dy_{24}Na_{44}$**) emu·K/mol at 1.8 K. The downward trend at high temperatures can be attributed to the thermal depopulation effect of the excited Stark sublevels of the Dy(III) ions,[60-63] while the decrease at low temperatures suggests the presence of possible antiferromagnetic interaction between the Dy(III) ions.[64-66]

Under a strong magnetic field of 7 T at 2.0 K, the magnetization (Figure S16, inset) of **$Dy_{16}K_{12}$** and **$Dy_{24}Na_{44}$** reached 79.27 and 119.69 μ_B, respectively, both significantly lower than the saturation magnetization values for sixteen and twenty-four free Dy(III) ions ($g_J \times J = {}^4/_3 \times {}^{15}/_2 = 10\ \mu_B$ per Dy(III) ion). This difference is mainly due to the magnetic anisotropy of the Dy(III) ions and their crystal field effects, which together result in the elimination of the sixteen-fold degenerate of the $^6H_{15/2}$ ground state.[67] The experimental data on magnetization as a function of external field could not be normalized to a single master curve, further confirming the presence of significant magnetic anisotropy in both compounds or/and the existence of low-lying excited states.[68-71] For **$Dy_{16}K_{12}$**, a minor open hysteresis loop with a coercive field of 0.15 kOe was observed at 1.8 K. This hysteresis loop gradually narrowed with increasing temperature and completely disappeared at 2.9 K. In stark contrast, **$Dy_{24}Na_{44}$** exhibited a characteristic butterfly-shaped hysteresis loop at 1.8 K that persisted until 2.6 K before vanishing (Figure S17). This behavior aligns with the rapid quantum tunneling of magnetization process.[72-75] The significant difference in hysteresis loop characteristics between the two compounds most likely arises from the complex magnetic interactions induced by the dramatic increase in nuclearity.

***AC* magnetic properties.** High-nuclearity lanthanide clusters generally exhibit highly symmetric topologies, where the overall magnetic anisotropy is frequently canceled out, rendering the detection of slow relaxation phenomena in magnetization particularly challenging.[51,59,76] Within a static magnetic field range of 0 T to 0.4 T, we conducted nine sets of variable-frequency (1.0-999 Hz) ac magnetic susceptibility measurements on powdered microcrystalline samples of compounds **$Dy_{16}K_{12}$** and **$Dy_{24}Na_{44}$** at a temperature of 2 K (Figure 3a and S18a). The measurement results revealed that under zero-field conditions, **$Dy_{16}K_{12}$** exhibited a significant out-of-phase susceptibility (χ_M'') in the high-frequency region, although no distinct peak was observed. As the magnetic field increased, the high-frequency χ_M'' signal shifted notably towards the low-frequency direction, reaching an optimal value at a magnetic field strength of 0.2 T, which corresponded to a faster relaxation phase (FR), after which the signal intensity gradually weakened. Meanwhile, the low-frequency χ_M'' signal continued to increase with the enhancement of the magnetic field, displaying a slower relaxation phase (SR), but no peak shift phenomenon was observed. The emergence of this two-step relaxation process is not coincidental; it can be attributed to the presence of multiple spin centers in **$Dy_{16}K_{12}$**, as well as the complex weak magnetic interactions among the Dy(III) ions. We employed the CC-FIT2 code[77-79] based on the modified Debye function (eqn 1) to fit and analyze the Cole-Cole data (Figure 3b, inset and Table S10), extracting the magnetic field-dependent relaxation time parameters τ_{SR} and τ_{FR}.

$$\chi_{ac}(\omega) = \chi_S + \sum_k \frac{\Delta\chi_k}{1+(i\omega\tau)^{(1-\alpha_k)}} \quad (1)$$
$$\chi_S = \sum_k \chi_{S,k};\ \Delta\chi_k = \chi_{T,k} - \chi_{S,k}$$

In this function, the sum of the adiabatic susceptibilities for the two magnetic relaxation processes is denoted by $\chi_S = \chi_{S1} + \chi_{S2}$. The difference between the isothermal susceptibility ($\chi_{T,k}$) and the adiabatic susceptibility ($\chi_{S,k}$) for each magnetic relaxation process is denoted by $\Delta\chi_k$. The α represents the distribution coefficient of the relaxation time τ, while ω is expressed as $2\pi\nu$.[80] As the dc field increases to 0.4 T, τ_{FR} increases monotonically, while τ_{SR} reaches its longest relaxation time at 0.2 T and then decreases with further increases in the dc field (Figure 3b). This suggests that applying a dc field can effectively slow down the magnetic relaxation process.

The magnetic field-dependent ac magnetic susceptibility of **$Dy_{24}Na_{44}$** shows significant differences compared to **$Dy_{16}K_{12}$** (Figure 3c and S18b). The χ_M'' signal for **$Dy_{24}Na_{44}$** exhibits a pronounced peak-shift in the high-frequency region. However, as the magnetic field increases, the intensity of this high-frequency signal gradually weakens and shifts to higher frequency regions, with no low-frequency signals ever appearing. This phenomenon is consistent with the characteristics of a one-step slow magnetic relaxation process, primarily resulting from the cancellation of magnetic anisotropy in its highly symmetric three-shell barrel-shaped topology. The extracted magnetic field-dependent relaxation time parameters exhibit a monotonically decreasing trend (Figure 3d and Table S11), indicating that the application of the dc field on the system is limited,[81] further confirming that the tunneling of **$Dy_{24}Na_{44}$** is weaker than that of **$Dy_{16}K_{12}$**.

To further investigate the complex magnetic dynamic behavior of **$Dy_{16}K_{12}$**, the frequency-dependent ac susceptibility was measured in the temperature range from 1.8 K to 18 K under zero dc field (Figure 3e, 3f and S19). The $\chi_M''(\nu)$ curves did not exhibit a peak even at the highest frequency of 999 Hz, indicating that there is no significant barrier in the relaxation process. This is primarily attributed to zero-field tunneling caused by intramolecular hyperfine coupling or dipole-dipole interactions.[82] The Cole-Cole plot was fitted using the generalized Debye model (Figure 3g and Table S12), yielding the relaxation time. The natural logarithm of the relaxation time gradually deviates from a linear relationship as the temperature

View Article Online
DOI: 10.1039/D5QI01402D

decreases (Figure 3h), which is a typical manifestation of the relaxation pathways involving Raman, direct, and tunneling processes. Applying eqn (2) provided well fits for the ln(τ) versus 1/T data, resulting in the following parameters: C = 8.60(5) × 10^{-2} s^{-1} $K^{-7.22}$, n = 7.22(4), A = 5.49(6) × 10^{-3} s^{-1} K^{-1}, and τ_{tunnel} = 6.32(2) × 10^{-4} s (Table 3).

$$\ln \tau = -\ln(CT^{n} + AT + \tau^{-1}_{tunnel}) \quad (2)$$

Considering the Raman, direct, and tunneling processes of Ln-SMMs, parameters C, n, A and τ_{tunnel} are all within reasonable ranges.[83] For the sake of caution, an Orbach process was not applied. We have also performed isolated fitting for the three relaxation mechanisms of the relaxation time, and the relevant parameters are summarized in Table S7.

To investigate the field-induced slow relaxation of **$Dy_{16}K_{12}$**, we applied an optimal dc field of 0.2 T (Figure 3i, 3j and S20). The $\chi_M''(\nu)$ curve exhibited a distinct double-peak feature: the high-frequency peak shifted significantly with increasing temperature, displaying SR characteristics; whereas the low-frequency peak only diminished in intensity with rising temperature but remained in the same position, demonstrating FR characteristics, which is a typical representation of tunneling.[84] By fitting a series of asymmetric Cole-Cole plots using eq 1 (Figure 3k and Table S13), we obtained two sets of parameters, α_{SR} and α_{FR}, with values ranging from 0.28(1) to 0.44(5) and 0.40(3) to 0.51(8), respectively, indicating a broad distribution of relaxation times for each relaxation phase.[79] The fast relaxation parameter τ_{SR} is approximately an order of magnitude faster than the slow relaxation parameter τ_{FR}, further confirming the significant difference between the direct process and the tunneling process (Figure 3l). When evaluating the SR process, we comprehensively considered the Orbach, Raman, direct, and tunneling processes, and fitted the relaxation time using eq 3, yielding the results: U_{eff} = 23.39(6) K, τ_o = 1.65(4) × 10^{-7} s, C = 4.58(4) × 10^{-2} s^{-1} $K^{-6.91}$, n = 6.91(4), A = 9.82(1) × 10^{-3} s^{-1} K^{-1} and τ_{tunnel} = 7.86(4) × 10^{-4} s (Table 3).

$$\ln \tau = -\ln\left(\tau_0^{-1}\exp\left(-\frac{U_{eff}}{k_B T}\right) + CT^{n} + AT + \tau_{tunnel}^{-1}\right) \quad (3)$$

All six parameters fell within acceptable ranges for fitting Ln-SMMs,[85] and the previously mentioned data were fitted independently using four distinct mechanisms. The resulting fitting outcomes are presented in Table S8.

Compared to the zero-field slow relaxation process of **$Dy_{16}K_{12}$**, the $\chi_M''(\nu)$ curve for **$Dy_{24}Na_{44}$** shows significant peaks that vary with temperature. The highest peak occurs at 454 Hz at a temperature of 1.8 K, and as the temperature rises, the peak gradually shifts towards higher frequencies; by 5.0 K, the peak moves out of the measuring window (Figure 3m-3p and S21). The low temperature of the peak indicates that the slow relaxation pathway is mainly governed by Raman, direct, and tunneling processes. The parameter value of a is approximately 0.16, clearly showing that the relaxation time distribution is narrow.[60] Fitting the relaxation time data (eq 2) yields the parameters: C = 4.05(8) × 10^{-2} s^{-1} $K^{-6.24}$, n = 6.24(6), A = 8.49(5) × 10^{-3} s^{-1} K^{-1} and τ_{tunnel} = 8.91(2) × 10^{-4} s (Table 3 and S14). The obtained parameters fall within a reasonable range for analyzing Ln-SMMs, and the fitting parameters for the three isolated processes are presented in Table S9.

Table 3. Parameters used to fit temperature-dependent relaxation times for **$Dy_{16}K_{12}$** and **$Dy_{24}Na_{44}$** extracted from ac magnetic susceptibility.

Compound	**$Dy_{16}K_{12}$**			**$Dy_{24}Na_{44}$**
H_{dc} (T)	**0**	**0.2**		**0**
Magnetic relaxation channel	**slower**	**slower**	**faster**	**slower**
τ_o (s)	--	1.65(4) × 10^{-7}	--	--
U_{eff} (K)	--	23.39(6)	--	--
C (s^{-1} K^{-n})	8.60(5) × 10^{-2}	4.58(9) × 10^{-2}	--	4.05(8) × 10^{-2}
n	7.22(4)	6.91(4)	--	6.24(6)
τ_{tunnel} (s)	6.32(2) × 10^{-4}	7.86(4) × 10^{-4}	1.03(5) × 10^{-4}	8.91(2) × 10^{-4}
A (s^{-1} K^{-1})	5.49(6) × 10^{-3}	9.82(1) × 10^{-3}	--	8.49(5) × 10^{-3}

A comparative analysis of the magnetic properties of the three-shell cyclic core structure of **$Dy_{16}K_{12}$** and the three-layer barrel-shaped core structure of **$Dy_{24}Na_{44}$** reveals significant differences between the two, highlighting a close relationship between molecular structure and magnetic properties. Static magnetic susceptibility indicates that below 56 K, both compounds exhibit antiferromagnetic interactions among the Dy(III) ions within the molecules. However, it is noteworthy that within the temperature range of 300 K to 56 K, the $\chi_M T$ curve of **$Dy_{16}K_{12}$** shows only a slight decrease, while **$Dy_{24}Na_{44}$** demonstrates a significant reduction. This difference may be related to the numerous aggregates of the Dy(III) ions. AC magnetic susceptibility reveals significant differences in the relaxation dynamics of the two compounds: At zero applied field, compound **$Dy_{16}K_{12}$** shows no clear out-of-phase peak at 1.8 K, while compound **$Dy_{24}Na_{44}$** exhibits a distinct high-frequency peak below 5.0 K. Upon applying a small dc field of 0.2 T, compound **$Dy_{16}K_{12}$** displays a two-step relaxation process, whereas compound **$Dy_{24}Na_{44}$** remains stable. These disparities primarily arise from two key structural factors: Firstly, during the structural transition from compound **$Dy_{16}K_{12}$** to compound **$Dy_{24}Na_{44}$**, there are numerous changes in the coordination geometry of the Dy^{III} ions. Additionally, the strong intermolecular hydrogen bonding and π-π stacking

DOI: 10.1039/D5QI01403D

interactions in compound $Dy_{16}K_{12}$ (resulting in a Dy···Dy distance approximately 2.96 Å shorter than in the latter) sharply contrast with the weaker intermolecular interactions in compound $Dy_{24}Na_{44}$. These structural differences affect the magnetic anisotropy of the system and ultimately lead to the distinctly different magnetic relaxation behaviors of the two compounds.

Conclusions

In summary, this work successfully constructed complex relaxation dynamics of disc-shaped $Dy_{16}K_{12}$ and barrel-shaped $Dy_{24}Na_{44}$ phosphonates by employing a mixed anion template strategy, along with terminally modifiable C_2-symmetric double hydrazone-based co-ligands. The flexibility of the naphthyl group in the phosphonate ligand plays a crucial regulatory role during the assembly process. A significant breakthrough was achieved by substituting sodium carbonate for potassium hydroxide, resulting in the aggregation of large negative charges within the cages, thereby yielding high-nuclearity coordination clusters. The hexacontaoctanuclear $Dy_{24}Na_{44}$ compound contains up to twenty-five carbonate and two chloride anions. Both clusters not only exhibit complex slow relaxation behaviors but also elucidate the regulatory mechanisms of relaxation dynamics through systematic structure-property relationship analyses. This synthetic strategy, which integrates phosphonate, carbonate, halide, hydrazone, and strongly uniaxial anisotropic lanthanide ions, offers a new approach for developing high-nuclearity three-shell systems with fascinating and multifunctional properties.

Author contributions

H. T. designed and supervised the research; C. W., Y. L., X. L. and H. L. synthesized and characterized the complexes; H. T. L. and C. W. performed the crystallographic investigation; H. T. performed the magnetometric measurements and analyses; H. Y. L. and H. T. wrote the manuscript with input from all authors.

Data availability

The data supporting this article have been included as part of the ESI.† Crystallographic data have been deposited at the CCDC under CCDC 2456379–2456380† and can be obtained from https://www.ccdc.cam.ac.uk/structures/.

Conflicts of interest

There are no conflicts to declare.

Acknowledgements

This work was supported by the Shandong Provincial Natural Science Foundation (ZR2022MB102) and the Natural Science Foundation of China (22461006), and additional financial support was provided by Liaocheng University (318051722 and 318012022).

Notes and references

1 T. R. Cook, V. Vajpayee, M. H. Lee, P. J. Stang and K.-W. Chi, Biomedical and Biochemical Applications of Self-Assembled Metallacycles and Metallacages, *Acc. Chem. Res.*, 2013, **46**, 2464–2474.
2 Q.-H. Ling, Z.-C. Lou, L. Zhang, T. Jin, W.-T. Dou, H.-B. Yang and L. Xu, Supramolecular cage-mediated cargo transport, *Chem. Soc. Rev.*, 2024, **53**, 6042–6067.
3 A. V. Virovets, E. Peresypkina and M. Scheer, Structural Chemistry of Giant Metal Based Supramolecules, *Chem. Rev.*, 2021, **121**, 14485-14554.
4 D. Fujita, Y. Ueda, S. Sato, N. Mizuno, T. Kumasaka and M. Fujita, Self-Assembly of Tetravalent Goldberg Polyhedra from 144 Small Components, *Nature*, 2016, **540**, 563–566.
5 M. Nyman and G. Deblonde, Metal-oxide cage traps radioactive element, *Nature*, 2023, **616**, 438–440.
6 H. Gan, N. Xu, C. Qin, C. Sun, X. Wang and Z. Su, Equi–Size Nesting of Platonic and Archimedean Metal-Organic Polyhedra into a Twin Capsid, *Nat. Commun.*, 2020, **11**, No. 4103.
7 A. V. Virovets, E. Peresypkina and M. Scheer, Structural Chemistry of Giant Metal Based Supramolecules, *Chem. Rev.*, 2021, **121**, 14485-14554.
8 X.-M. Luo, Y.-K. Li, X.-Y. Dong and S.-Q. Zang, Platonic and Archimedean solids in discrete metal-containing clusters, *Chem. Soc. Rev.*, 2023, **52**, 383–444.
9 N.-F. Li, X.-M. Luo, J. Wang, J.-L. Wang, H. Mei, Y. Song and Y. Xu, Largest 3d-4f 196-nuclear $Gd_{158}Co_{38}$ clusters with excellent magnetic cooling, *Sci. China Chem.*, 2022, **65**, 1577–1583.
10 X.-Z. Li, C.-B. Tian, Q.-F. Sun, Coordination-Directed Self-Assembly of Functional Polynuclear Lanthanide Supramolecular Architectures, *Chem. Res.*, 2022, **122**, 6374–6458.
11 L. Münzfeld, S. Gillhuber, A. Hauser, S. Lebedkin, P. Hädinger, N. D. Knöfel, C. Zovko, M. T. Gamer, F. Weigend, M. M. Kappes and P. W. Roesky, Synthesis and properties of cyclic sandwich compounds, *Nature*, 2023, **620**, 92–96.
12 X.-Y. Li, H.-F. Su, Q.-W. Li, R. Feng, H.-Y. Bai, H.-Y. Chen, J. Xu and X.-H. Bu, A Giant Dy_{76} Cluster: A Fused Bi-Nanopillar Structural Model for Lanthanide Clusters. *Angew. Chem. Int. Ed.*, 2019, **58**, 10184–10188.
13 I. Colliard and M. Nyman, Ce^{IV}_{70} Oxosulfate Rings, Frameworks, Supramolecular Assembly, and Redox Activity, *Angew. Chem. Int. Ed.*, 2021, **60**, 7308–7315.
14 J.-Y. He, Y. Wang, X. Chen, W.-P. Chen, G. Zhou and Y.-Z. Zheng, Air and Thermally Stable Fluoride Bridged Rare-Earth Clusters Showing Intense Photoluminescence and Potential LED Application, *Adv. Mater.*, 2024, **36**, 2406882.
15 S. P. K. Panguluri, E. Jourdain, P. Chakraborty, S. Klyatskaya, M. M. Kappes, A. M. Nonat, L. J. Charbonniere and M. Ruben, Yb-to-Eu Cooperative Sensitization Upconversion in a Multifunctional Molecular Nonanuclear Lanthanide Cluster in Solution, *J. Am. Chem. Soc.*, 2024, **146**, 13083–13092.
16 W. Huang, Q. Yang, W. Chen and Z. Zheng, Anion-Guided Hierarchical Assembly of Heterometallic Clusters, *J. Am. Chem. Soc.*, 2025, **147**, 5572-5576.
17 A. Clearfield, Metal phosphonate chemistry, *Prog. Inorg. Chem.*, 1997, **47**, 371–510.
18 J.-G. Mao, Structures and luminescent properties of lanthanide phosphonates, *Coord. Chem. Rev.*, 2007, **251**, 1493–1520.

19 A. Clearfield and K. Demadis, Metal Phosphonate Chemistry: From Synthesis to Applications; Royal Society of Chemistry, 2011.

20 A. Banerjee, B. S. Bassil, G.-V. Röschenthaler and U. Kortz, Diphosphates and diphosphonates in polyoxometalate chemistry, *Chem. Soc. Rev.*, 2012, **41**, 7590−7604.

21 R. J. Blagg, L. Ungur, F. Tuna, J. Speak, P. Comar, D. Collison, W. Wernsdorfer, E. J. L. McInnes, L. F. Chibotaru and R. E. P. Winpenny, Magnetic relaxation pathways in lanthanide single-molecule magnets, *Nat. Chem.*, 2013, **5**, 673−678.

22 J. Goura and V. Chandrasekhar, Molecular Metal Phosphonates, *Chem. Rev.*, 2015, **115**, 6854−6965.

23 S.-S. Bao and L.-M. Zheng, Magnetic materials based on 3d metal phosphonates, *Coord. Chem. Rev.*, 2016, **319**, 63−85.

24 G. Yücesan, Y. Zorlu, M. Stricker and J. Beckmann, Metal-Organic Solids Derived from Arylphosphonic Acids, *Coord. Chem. Rev.*, 2018, **369**, 105−122.

25 S.-S. Bao, M.-F. Qin and L.-M. Zheng, Metal phosphonates incorporating metalloligands: assembly, structures and properties, *Chem. Commun.*, 2020, **56**, 12090.

26 X.-D. Huang, X.-F. Ma and L.-M. Zheng, Photo-responsive Single-Molecule Magnet Showing 0D to 1D Single-Crystal-to-Single-Crystal Structural Transition and Hysteresis Modulation, *Angew. Chem. Int. Ed.*, 2023, **62**, No. e202300088.

27 D. D. A. Jayasinghe, Y. Chen, J. Li, J. M. Rogacka, M. Kippax−Jones, W. Lu, S. Sapchenko, J. Yang, S. Chansai, T. Zhou, L. Guo, Y. Ma, L. Dong, D. Polyukhov, L. Shan, Y. Han, D. Crawshaw, X. Zeng, Z. Zhu, L. Hughes, M. D. Frogley, P. Manuel, S. Rudić, Y. Cheng, C. Hardacre, M. Schröder and S. Yang, A Flexible Phosphonate Metal–Organic Framework for Enhanced Cooperative Ammonia Capture, *J. Am. Chem. Soc.*, 2024, **146**, 32040-32048.

28 C. Ribeiro, B. Tan, F. Figueira, R. F. Mendes, J. Calbo, G. Valente, P. Escamilla, F. A. A. Paz, J. Rocha, M. Dincă and M. Souto, Mixed Ionic and Electronic Conductivity in a Tetrathiafulvalene-Phosphonate Metal-Organic Framework, *J. Am. Chem. Soc.*, 2025, **147**, 63-68.

29 S. Bian, J. Jia and Q. Wang, High-Nuclearity Silver Clusters Templated by Carbonates Generated from Atmospheric Carbon Dioxide Fixation, *J. Am. Chem. Soc.*, 2009, **131**, 3422–3423.

30 S. I. Swamy, J. Bacsa, J. T. A. Jones, K. C. Stylianou, A. Steiner, L. K. Ritchie, T. Hasell, J. A. Gould, A. Laybourn, Y. Z. Khimyak, D. J. Adams, M. J. Rosseinsky and A. I. Cooper, A Metal–Organic Framework with a Covalently Prefabricated Porous Organic Linker, *J. Am. Chem. Soc.*, 2010, **132**, 12773–12775.

31 J. S. Silvia and C. C. Cummins, Binding, release, and functionalization of CO_2 at a nucleophilic oxo anion complex of titanium, *Chem. Sci.*, 2011, **2**, 1474-1479.

32 K. Sokołowski, W. Bury, I. Justyniak, D. Fairen-Jimenez, K. Sołtys, D. Prochowicz, S. Yang, M. Schröder and J. Lewiński, Permanent Porosity Derived From the Self-Assembly of Highly Luminescent Molecular Zinc Carbonate Nanoclusters, *Angew. Chem. Int. Ed.*, 2013, **52**. 13414–13418.

33 V. Velasco, D. Aguilà, L. A. Barrios, I. Borilovic, O. Roubeau, J. Ribas-Ariño, M. Fumanal, S. J. Teat and G. Aromí, New coordination features; a bridging pyridine and the forced shortest non-covalent distance between two CO_3^{2-} species, *Chem. Sci.*, 2015, **6**, 123–131.

34 K. Sołtys-Brzostek, M. Terlecki, K. Sokołowski and J. Lewinski, Chemical fixation and conversion of CO_2 into cyclic and cage-type metal carbonates, *Coord. Chem. Rev.*, 2017, **334**, 199−231.

35 X.-Y. Zheng, X.-J. Kong, Z. Zheng, L.-S. Long and L.-S. Zheng, High-Nuclearity Lanthanide-Containing Clusters as Potential Molecular Magnetic Coolers**,** *Acc. Chem. Res.*, 2018, **51**, 517−525.

36 Z. Wang, R. K. Gupta, G.-G. Luo and D. Sun, Recent Progress in Inorganic Anions Templated Silver Nanoclusters: Synthesis, Structures and Properties, *Chem. Rec.*, 2020, **20**, 389−402.

37 W. Huang, W. Chen, Q. Bai, Z. Zhang, M. Feng and Z. Zheng, Anion-Guided Stepwise Assembly of High-Nuclearity Lanthanide Hydroxide Clusters, *Angew. Chem. Int. Ed.*, 2022, **61**, No. e202205385.

38 J. K. Nath and R. A. Borah, lanthanide cluster formed by fixing atmospheric CO_2 to carbonate: a molecular magnetic refrigerant and photoluminescent material, *J. Chem. Sci.*, 2023, **135**, 58.

39 N. Xu, W. Chen, Y.-S. Ding and Z. Zheng, A Cubic Tinkertoy-like Heterometallic Cluster with a Record Magnetocaloric Effect, *J. Am. Chem. Soc.*, 2024, **146**, 9506−9511.

40 Y.-N. Guo, X.-H. Chen, S. Xue and J. Tang, Molecular Assembly and Magnetic Dynamics of Two Novel Dy_6 and Dy_8 Aggregates, *Inorg. Chem.*, 2012, **51**, 4035–4042.

41 A. S. R. Chesman, D. R. Turner, S. K. Langley, B. Moubaraki, K. S. Murray, G. B. Deacon and S. R. Batten, Synthesis and Structure of New Lanthanoid Carbonate "Lanthaballs", *Inorg. Chem.*, 2015, **54**, 792–800.

42 I. P. Beletskaya and M. A. Kazankova, Catalytic Methods for Building up Phosphorus-Carbon Bond, Russ. *J. Org. Chem.*, 2002, **38**, 1391−1430.

43 H. Tian and L.-M. Zheng, Cyclic Lanthanide-based Molecular Clusters: Assembly and Single Molecule Magnet Behavior, *Acta Chim. Sin.*, 2020, **78**, 34−55.

44 S. Alvarez, P. Alemany, D. Casanova, J. Cirera, M. Llunell and D. Avnir, Shape maps and polyhedral interconversion paths in transition metal chemistry, *Coord. Chem. Rev.*, 2005, **249**, 1693−1708.

45 D. Casanova, M. Llunell, P. Alemany and S. Alvarez, The Rich Stereochemistry of Eight-Vertex Polyhedra: A Continuous Shape Measures Study, *Chem.-Eur. J.*, 2005, **11**, 1479−1494.

46 B. Moulton, J. J. Lu, R. Hajndl, S. Hariharan, M. J. Zaworotko, Crystal Engineering of a Nanoscale Kagomé Lattice, *Angew. Chem. Int. Ed.*, 2002, **41**, 2821−2824.

47 A. Müller, E. Beckmann, H. Bögge, M. Schmidtmann and A. Dress, Inorganic Chemistry Goes Protein Size: A Mo368 Nano-Hedgehog Initiating Nanochemistry by Symmetry Breaking, *Angew. Chem. Int. Ed.*, 2002, **41**, 1162-1167.

48 M. Fondo, N. Ocampo, A. M. García-Deibe, R. Vicente, M. Corbella, M. R. Bermejo and J. Sanmartín, Self-Assembly of a Tetranuclear Ni_4 Cluster with an S = 4 Ground State: The First 3*d* Metal Cluster Bearing a μ_4-η^2:η^2-*O*,*O* Carbonate Ligand, *Inorg. Chem.*, 2006, **45**, 255−262.

49 L. Addadi, Z. Berkovitch-Yellin, I. Weissbuch, J. van Mil, L. J. W. Shimon, M. Lahav and L. Leiserowitz, Growth and Dissolution of Organic Crystals with "Tailor-Made" Inhibitors—Implications in Stereochemistry and Materials Science, *Angew. Chem. Int. Ed.*, 1985, **24**, 466−485.

50 I. Weissbuch, R. Popovitz-Biro, M. Lahav and L. Leiserowitz, Understanding and Control of Nucleation, Growth, Habit, Dissolution and Structure of Two- and Three-dimensional Crystals using 'Tailor-made' Auxiliaries, *Acta Crystallogr. Sect. B*, 1995, **51**, 115−148.

51 D. D'Alessio, A. N. Sobolev, B. W. Skelton, R. O. Fuller, R. C. Woodward, N. A. Lengkeek, B. H. Fraser, M. Massi and M. I. Ogden, Lanthanide "Bottlebrush" Clusters: Remarkably Elongated Metal–Oxo Core Structures with Controllable Lengths, *J. Am. Chem. Soc.*, 2014, **136**, 15122−15125.

52 D. N. Woodruff, R. E. P. Winpenny and R. A. Layfield, Lanthanide Single-Molecule Magnets, *Chem. Rev.*, 2013, **113**, 5110−5148.

53 J. Dong, P. Cui, P.-F. Shi, P. Cheng and B. Zhao, Ultrastrong Alkali-Resisting Lanthanide-Zeolites Assembled by [Ln_{60}] Nanocages, *J. Am. Chem. Soc.*, 2015, **137**, 15988−15991.

54 T. P. Latendresse, N. S. Bhuvanesh and M. Nippe, Hard Single-Molecule Magnet Behavior by a Linear Trinuclear Lanthanide−[1]Metallocenophane Complex, *J. Am. Chem. Soc.*, 2017, **139**, 14877−14880.

55 B. S. Dolinar, D. I. Alexandropoulos, K. R. Vignesh, T. James and K. R. Dunbar, Lanthanide Triangles Supported by Radical Bridging Ligands, *J. Am. Chem. Soc.*, 2018, **140**, 908−911.

56 N. Mavragani, D. Errulat, D. A. Galico, A. A. Kitos, A. Mansikkamaki and M. Murugesu, Radical-Bridged Ln_4 Metallocene Complexes with Strong Magnetic Coupling and a Large Coercive Field, *Angew. Chem. Int. Ed.*, 2021, **60**, 24206-24213.

57 Y. Duan, L. E. Rosaleny, J. T. Coutinho, S. Giménez-Santamarina, A. Scheie, J. J. Baldoví, S. Cardona-Serra and A. Gaita-Ariño, Data-driven design of molecular nanomagnets, *Nat. Commun.*, 2022, **13**, 7626.

58 A. P. Orlova, M. G. Bernbeck and J. D. Rinehart, Designing Quantum Spaces of Higher Dimensionality from a Tetranuclear Erbium-Based Single-Molecule Magnet, *J. Am. Chem. Soc.*, 2024, **146**, 23417−23425.

59 M.-T. Chen, Q.-F. Xu, M. Aibibula, X.-J. Kong, L.-S. Long and L.-S. Zheng, High-Nuclearity $Ln_{210}Al_{140}$ Clusters: Neonates of Open Hollow Dodecahedral Cage Families, *J. Am. Chem. Soc.*, 2024, **146**, 22134−22139.

60 J. Tang, I. Hewitt, N. T. Madhu, G. Chastanet, W. Wernsdorfer, C. E. Anson, C. Benelli, R. Sessoli and A. K. Powell, Dysprosium Triangles Showing Single-Molecule Magnet Behavior of Thermally Excited Spin States, *Angew. Chem. Int. Ed.*, 2006, **45**, 1729−1733.

61 J. D. Rinehart and J. R. Long, Exploiting single-ion anisotropy in the design of f-element single-molecule magnets, *Chem. Sci.*, 2011, **2**, 2078−2085.

62 J.-L. Liu, Y.-C. Chen and M.-L. Tong, Symmetry strategies for high performance lanthanide-based single-molecule magnets, *Chem. Soc. Rev.*, 2018, **47**, 2431−2453.

63 P. Zhang, R. Nabi, J. K. Staab, N. F. Chilton and S. Demir, Taming Super-Reduced Bi_2^{3-} Radicals with Rare Earth Cations, *J. Am. Chem. Soc.*, 2023**, 145**, 9152-9163.

64 C. A. Gould, K. R. McClain, D. Reta, J. G. C. Kragskow, D. A. Marchiori, E. Lachman, E.-S. Choi, J. G. Analytis, R. D. Britt, N. F. Chilton, B. G. Harvey and J. R. Long, Ultrahard magnetism from mixed-valence dilanthanide complexes with metal-metal bonding, *Science*, 2022, **375**, 198-202.

65 J. M. Van Raden, D. I. Alexandropoulos, M. Slota, S. Sopp, T. Matsuno, A. L. Thompson, H. Isobe, H. L. Anderson and L. Bogani, Singly and Triply Linked Magnetic Porphyrin Lanthanide Arrays, *J. Am. Chem. Soc.*, 2022, **144**, 8693-8706.

66 Z. Zhu, S. Paul, C. Zhao, J. Wu, X. Ying, L. Ungur, W. Wernsdorfer, F. Meyer and J. Tang, Record Quantum Tunneling Time in an Air-Stable Exchange-Bias Dysprosium Macrocycle, *J. Am. Chem. Soc.*, 2024, **146**, 18899−18904.

67 S. Osa, T. Kido, N. Matsumoto, N. Re, A. Pochaba and J. Mrozinski, *J. Am. Chem. Soc.*, 2004, **126**, 420–421.

68 C. A. P. Goodwin, F. Ortu, D. Reta, N. F. Chilton and D. P. Mills, Molecular magnetic hysteresis at 60 kelvin in dysprosocenium, *Nature*, 2017, **548**, 439-442.

69 F.-S. Guo, B. M. Day, Y.-C. Chen, M.-L. Tong, A. Mansikkamäki and R. A. Layfield, Magnetic hysteresis up to 80 kelvin in a dysprosium metallocene single-molecule magnet, *Science*, 2018, **362**, 1400-1403.

70 C. Gao, A. Genoni, S. Gao, S. Jiang, A. Soncini and J. Overgaard, Observation of the Asphericity of 4f-electron Density and its Relation to Themagnetic Anisotropy Axis in Single-molecule Magnets, *Nat. Chem.*, 2020, **12**, 213−219.

71 M. Liu, Y.-C. Chen, A. Mondal, H. Wang, M.-L. Tong, R. A. Layfield and F.-S. Guo, η^6-Benzene Tetra-Anion Complexes of Early and Late Rare-Earth Metals, *J. Am. Chem. Soc.*, 2025, **147**, 11359−11367.

72 M. E. Boulon, G. Cucinotta, S.-S. Liu, S.-D. Jiang, L. Ungur, L. F. Chibotaru, S. Gao and R. Sessoli, Angular-resolved magnetometry beyond triclinic crystals: out-of-equilibrium studies of Cp*ErCOT single-molecule magne, *Chem*, 2013, 19, 13726–13731.

73 Y.-S. Meng, S.-D. Jiang, B.-W. Wang and Song Gao, Understanding the Magnetic Anisotropy toward Single-Ion Magnets, *Acc. Chem. Res*., 2016, **49**, 2381−2389.

74 J. D. Hilgar, M. G. Bernbeck and J. D. Rinehart, Million-fold Relaxation Time Enhancement across a Series of Phosphino-Supported Erbium Single-Molecule Magnets, *J. Am. Chem. Soc.*, 2019, **141**, 1913–1917.

75 Z. Zhu, C. Zhao, T. Feng, X. Liu, X. Ying, X.-L. Li, Y.-Q. Zhang and J. Tang, Air-Stable Chiral Single-Molecule Magnets with Record Anisotropy Barrier Exceeding 1800 K, *J. Am. Chem. Soc.*, 2021, **143**, 10077–10082.

76 L. Qin, Y.-Z. Yu, P.-Q. Liao, W. Xue, Z. Zheng, X.- M. Chen and Y.-Z. Zheng, A. Molecular Water Pipe": A Giant Tubular Cluster {Dy_{72}} Exhibits Fast Proton Transport and Slow Magnetic Relaxation, *Adv. Mater.*, 2016, **28**, 10772−10779.

77 K. S. Cole and R. H. Cole, Dispersion and Absorption in Dielectrics I. Alternating Current Characteristics, *J. Chem. Phys.*, 1941, **9**, 341–351.

78 D. Reta and N. F. Chilton, Uncertainty estimates for magnetic relaxation times and magnetic relaxation parameters, *Phys. Chem. Chem. Phys.*, 2019, **21**, 23567–23575.

79 W. J. A. Blackmore, G. K. Gransbury, P. Evans, J. G. C. Kragskow, D. P. Mills and N. F. Chilton, Characterisation of magnetic relaxation on extremely long timescales, *Phys. Chem. Chem. Phys.*, 2023, **25**, 16735–16744.

80 Y.-X. Wang, Y. Ma, J.-S. Wang, Y. Yang, Guo, Y.-N.; Y.-Q. Zhang, K.-J. Jin, Y. Sun and P. Cheng. Ferroelectric Single-Molecule Magnet with Toroidal Magnetic Moments, *Adv. Sci.*, 2022, **9**, 2202979.

81 I. J. Hewitt, J. Tang, N. T. Madhu, C. E. Anson, Y. Lan, J. Luzon, M. Etienne, R. Sessoli and A. K. Powell, Coupling Dy_3 Triangles Enhances Their Slow Magnetic Relaxation, *Angew. Chem. Int. Ed.*, 2010, **49**, 6352−6356.

82 S. Demir, M. Nippe, M. I. Gonzalez and J. R. Long, Exchange coupling and magnetic blocking in dilanthanide complexes bridged by the multielectron redox-active ligand 2,3,5,6-tetra(2-pyridyl)pyrazine, *Chem. Sci.*, 2014, **5**, 4701–4711.

83 A. Lunghi, F. Totti, R. Sessoli and S. Sanvito, The role of anharmonic phonons in under-barrier spin relaxation of single molecule magnets, *Nat. Commun.*, 2017, **8**, 14620.

84 J. D. Rinehart, K. R. Meihaus and J. R. Long, Observation of a Secondary Slow Relaxation Process for the Field-Induced Single-Molecule Magnet $U(H_2BPz_2)_3$, *J. Am. Chem. Soc.*, 2010, **132**, 7572–7573.

85 A. H. Vincent, Y. L. Whyatt, N. F. Chilton and J. R. Long, Strong Axiality in a Dysprosium(III) Bis(borolide) Complex Leads to Magnetic Blocking at 65 K**,** *J. Am. Chem. Soc.*, 2023, **145**, 1572–1579.

View Article Online
DOI: 10.1039/D5QI01403D

The data supporting this article have been included as part of the ESI†. Crystallographic data have been deposited at the CCDC under CCDC 2456379–2456380† and can be obtained from https://www.ccdc.cam.ac.uk/structures/.